Ma, J., Dineva, S., Cesca, S., Heimann, S. (2018): Moment tensor inversion with three-dimensional sensor configuration of mining induced seismicity (Kiruna mine, Sweden). - *Geophysical Journal International*, *213*, 3, pp. 2147—2160.

DOI: http://doi.org/10.1093/gji/ggy115

Geophysical Journal International

Geophys. J. Int. (2018) **213,** 2147–2160
Advance Access publication 2018 March 22
GJI Seismology

doi: 10.1093/gji/ggy115

Moment tensor inversion with three-dimensional sensor configuration of mining induced seismicity (Kiruna mine, Sweden)

Ju Ma,[1,2] Savka Dineva,[2] Simone Cesca[3] and Sebastian Heimann[3]

[1] *Department of Mining Engineering, North China University of Science and Technology, Tangshan 063210, Hebei, China. E-mail: machoju@foxmail.com*
[2] *Department of Civil, Mining and Environmental Engineering, Luleå University of Technology, 97187 Luleå, Sweden*
[3] *GFZ German Research Centre for Geosciences Potsdam, D-14467 Potsdam, Germany*

Accepted 2018 March 21. Received 2018 March 19; in original form 2017 September 12

SUMMARY

Mining induced seismicity is an undesired consequence of mining operations, which poses significant hazard to miners and infrastructures and requires an accurate analysis of the rupture process. Seismic moment tensors of mining-induced events help to understand the nature of mining-induced seismicity by providing information about the relationship between the mining, stress redistribution and instabilities in the rock mass. In this work, we adapt and test a waveform-based inversion method on high frequency data recorded by a dense underground seismic system in one of the largest underground mines in the world (Kiruna mine, Sweden). A stable algorithm for moment tensor inversion for comparatively small mining induced earthquakes, resolving both the double-couple and full moment tensor with high frequency data, is very challenging. Moreover, the application to underground mining system requires accounting for the 3-D geometry of the monitoring system. We construct a Green's function database using a homogeneous velocity model, but assuming a 3-D distribution of potential sources and receivers. We first perform a set of moment tensor inversions using synthetic data to test the effects of different factors on moment tensor inversion stability and source parameters accuracy, including the network spatial coverage, the number of sensors and the signal-to-noise ratio. The influence of the accuracy of the input source parameters on the inversion results is also tested. Those tests show that an accurate selection of the inversion parameters allows resolving the moment tensor also in the presence of realistic seismic noise conditions. Finally, the moment tensor inversion methodology is applied to eight events chosen from mining block #33/34 at Kiruna mine. Source parameters including scalar moment, magnitude, double-couple, compensated linear vector dipole and isotropic contributions as well as the strike, dip and rake configurations of the double-couple term were obtained. The orientations of the nodal planes of the double-couple component in most cases vary from NNW to NNE with a dip along the ore body or in the opposite direction.

Key words: Induced seismicity; Seismic noise; Earthquake source observations.

1 INTRODUCTION

Event locations and magnitudes give limited insight into the mining induced seismicity. A deeper understanding of seismic hazard and its relation to the geological structures and local stresses can be enhanced by resolving the seismic moment tensor (MT) of mining induced earthquakes, which serves as a direct snapshot of the instantaneous deformation of the surrounding rock. When an earthquake occurs, the rock experiences some form of failure. The seismic MT describes whether the failure is shearing or tearing, if a change in volume occurred or some combination of these scenarios.

MTs are important because they completely describe the equivalent forces of a seismic source in a point source approximation with the exception of unit body forces radiation. The equivalent forces can be related to physical source models such as sudden relative displacement on a fault, rapidly propagating metastable phase transitions, a collapse of cavities due to phase transitions or sudden volume increase due to explosions (Jost & Herrmann 1989). In general, the MT is formally described by a symmetric tensor, which has as entries the generalized force couples (Aid & Richards 1980). It can be decomposed into an isotropic (ISO) term and a deviatoric one. Among the possible decompositions of the deviatoric term, the most used is by a double-couple (DC) and a compensated linear vector dipole (CLVD; Knopoff & Randall 1970; Julian *et al.* 1998; Vavryčuk 2015). The equivalent forces representing a sudden displacement on a fault plane correspond to a DC, while the slip

deviating off the fault plane is represented by a CLVD (Dufumier & Rivera 1997; Vavryčuk 2001).

The MT inversion problem can be described as the process of determining the source parameters according to the desired source model though the fit of seismic observations. Several source inversion approaches have been proposed in the past decades, fitting different kind of observations and models. The MT inversion problem, either limited to a pure DC representation, a deviatoric or a full moment tensor (FMT), has been performed in the past upon the comparison of various waveform features, including first motion polarities (e.g. Nakamura 2002), seismic waveforms (e.g. Vavryčuk & Kühn 2012), *P*- and *S*-wave amplitude ratios (e.g. Jechumtálová & Šílený 2005) and combination of spectral amplitudes or amplitude ratios with *P*-wave polarities (e.g. Li *et al.* 2011).

Significant improvements have been obtained by MT inversion methods based on full waveforms, which could be applied for a broad range of magnitudes down to the microseismic scale (Song & Toksöz 2011). As the name suggests, full-waveform data recorded on all components at each of the sensors are inverted to calculate the seismic MT. Data depend on both the source contribution and a path (propagation) contribution. The propagation effects can be removed by modelling the propagation of seismic waves between source and receiver locations as accurately as possible. Thus, to obtain a reliable source model, the space of the source parameters has to be investigated, synthetic seismograms to be generated for a number of source models and their fit to the observed data estimated and compared. Waveform inversion methodologies are often performed in the time domain (e.g. Vavryčuk & Kühn 2012). The alternative approach is carried out in the frequency domain, either by fitting amplitude spectra (Dahm & Krüger 1999; Cesca *et al.* 2006) or complex spectra (e.g. Cesca *et al.* 2008). The advantage of this type of methods is that, as long as care is taken to accurately model the Green's functions, the inversion relies on the full seismic observation and the MT can be better constrained.

The purpose of this study is to adapt and test the waveform inversion methodology (Cesca *et al.* 2010, 2013) on high frequency data recorded by a dense underground 3-D seismic system in one of the largest underground mines in the world (Kiruna mine, Sweden) by determining both the DC and FMT point source models. The application to the underground mining system requires an algorithm adaption, to account for the 3-D geometry of the monitoring system. A second challenge concerns the larger number of recordings, since more than 200 geophones are operational within the mine (Dineva & Boskovic 2017). A Green's function database (GFDB) is then constructed considering the source depth, sensor depth and epicentral distance, to be able to generate synthetic seismograms for sensors located below the source.

A set of MT inversions using synthetic data was carried out to test the effects of different factors, such as spatial network coverage (azimuthal gap), the number of sensors and the presence of noise. Moreover, we tested the influence of the accuracy of the known source parameters (source location, depth and origin time, which are used as input during inversion) on the inversion results. Finally, the MT inversion methodology was applied to eight real events chosen from mining block #33/34 that occurred between 2015 September 6 and 2016 January 22. Source parameters including scalar moment, magnitude, DC, CLVD and ISO contributions and the strike, dip and rake configurations of the DC term were obtained. In perspective, this application represents the first step with recommendations towards an automation of the inversion routine.

2 BACKGROUND

Kiirunavaara (Kiruna) iron ore mine, owned and operated by LKAB (Sweden), is one of the largest underground mines in the world. The deposit consists of a ∼4 km long, ∼80 m wide, tabular ore body of rich magnetite dipping 60° east. Mining started in 1898 as an open pit mine. In mid-1950, the mine started a transition to underground mining and passed to only underground mining in 1962. More substantial induced seismicity started in 2007–2008, when the deepest mining level was 907 m. Depths are referenced to a reference 0 m mining level, which corresponds to 237 m above the sea level (the highest level at the beginning of the mining production). All depths in the paper refer to mining level. By 2016, the mining production was at 1022–1079 m depth (around 785–845 m below surface). More than one billion tons of ore have been extracted since the beginning of mining. The average yearly production in recent years is 28 million tons. By 2016, the mine seismic monitoring system had 204 operational geophones, 87 of which triaxial, the largest underground seismic system in the world. The number of the deployed sensors (geophones with natural frequencies of 4.5 and 14 Hz) changed with time and increased with the production depth (Dineva & Boskovic 2017). The microseismic monitoring system is shown in Fig. 1.

3 MOMENT TENSOR INVERSION WITH 3-D SENSOR CONFIGURATION

For MT inversion in mining environment we adopted the *Kiwi tools* (Cesca *et al.* 2010), which can be used both for a time domain (waveform fit) and frequency domain (amplitude spectra fit) inversion using pre-calculated GFDBs. This inversion package has been successfully applied to study seismic sources of moderate and large earthquakes at local and regional distances (e.g. Cesca *et al.* 2010) and tested for automated routines at regional distances (Domingues *et al.* 2013). At a local scale (up to 3 km), it has been used to model coal mining induced seismicity (Sen *et al.* 2013). However, it has never been routinely applied so far to small events recorded at small distances (less than 500 m) with moment magnitude below 1.0 and frequency higher than 50 Hz. Moreover, this is its first application where a 3-D network geometry is considered.

3.1 Implementation for mining induced seismicity

Previously, the *Kiwi tools* only dealt with waveforms recorded by sensors located at the same depth (typically at the Earth's surface). However, in a mining environment, and specifically at the Kiruna mine, sensors are located in a 3-D configuration (all around the seismic source). In this case, the traditional inversion algorithm and the GFDB structure (Cesca *et al.* 2010) cannot be used directly. Considering a homogeneous velocity model, synthetic seismograms can be computed, depending geometrically on the relative source–receiver depth, the epicentral distance and the azimuth. Instead of using the free surface as the zero-depth reference and considering the absolute source depth, we consider a relative source depth (h') with respect to each sensor, as

$$h'_i = h_s - h_i, \tag{1}$$

where h_s is the depth of the source and h_i is the depth of the sensor i (as sketched in Fig. 2).

The original geometry (Fig. 2, left) is defined with one absolute source depth h_s and several absolute sensor depths h_i (with respect to the free surface). To compute the GFDB and the synthetic

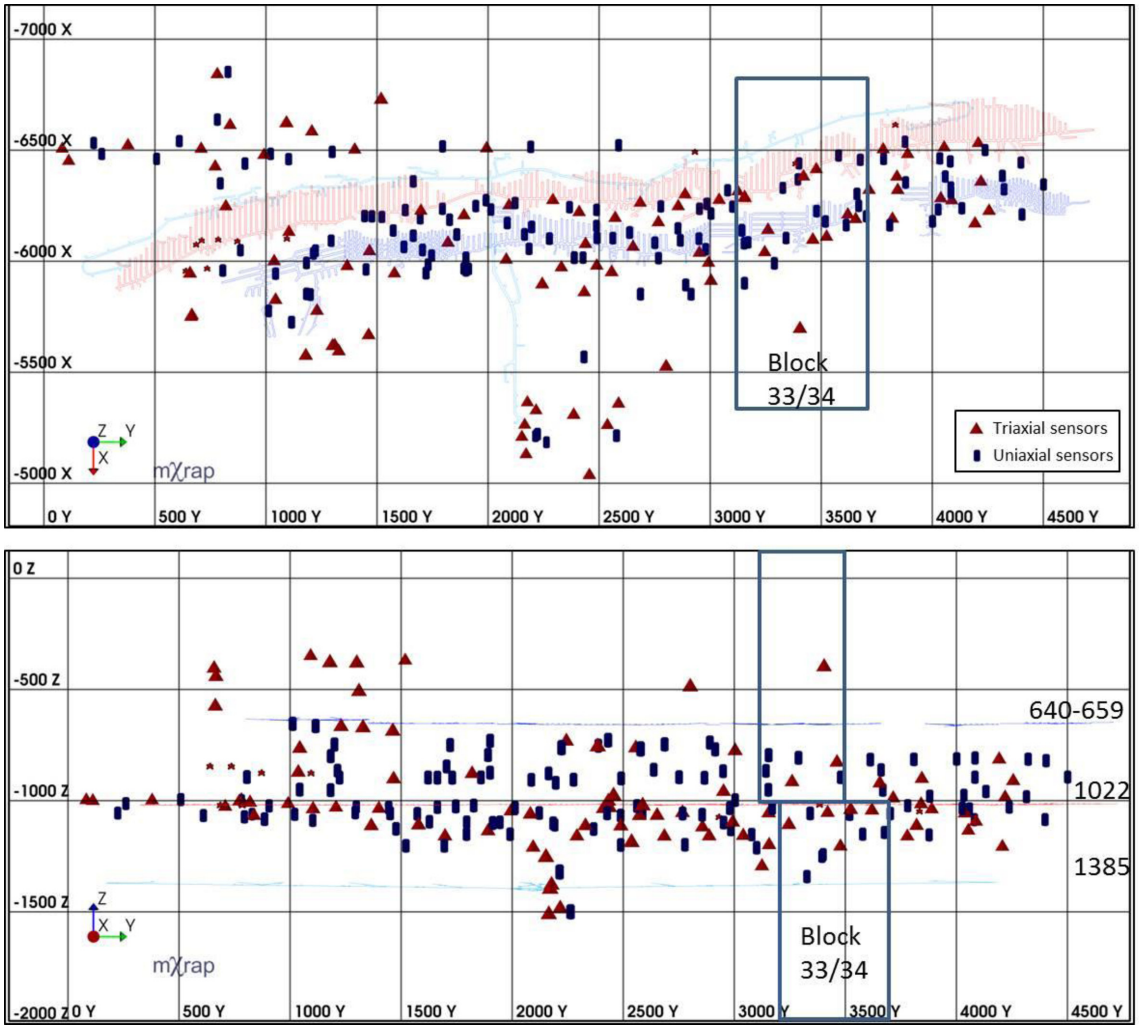

Figure 1. The Kiruna mine microseismic monitoring network in horizontal projection (*X*—E–W direction, *Y*—N–S direction) and vertical cross-section looking east. The pale blue and red stripes correspond to underground tunnels. Triangles and cylinders correspond to triaxial sensors and uniaxial sensors. The units along the axes are in m. The pale blue and red lines on top plot correspond to the outlines of production levels 640–659 and 1022. Plot with mXap software (Harris and Wesseloo, 2015)

seismograms, we replace the original geometry with an equivalent description (Fig. 2, right), which is defined with several relative source depths h_i' .

The *Kiwi tools* can efficiently compute the synthetic seismogram if the Green's functions are calculated in advance and stored in structured databases. The parameters for calculation of the GFDB here are chosen to correspond to the geometry of the seismic network in Kiruna mine and the relative locations of the seismic sources and seismic sensors. All calculations are done in the mine local coordinate system. Considering the expected range of mining depths at Kiruna mine (1000–1200 m) and the depth range of the seismic sensors (600–1400 m), we created a GFDB which allows building synthetic seismograms for sources with relative depth of 500 m below a sensor to 300 m above a sensor. The lateral spatial sampling, which controls the accuracy of the epicentral distance, is equal to 10 m. The Green's functions and the synthetic seismograms are sampled with 200 Hz. The parameters of the GFDB are given in Table 1. The homogeneous velocity model has *P*- and *S*-wave velocities 5500 m s^{-1} and 3107 m s^{-1}, respectively, and density 2700 kg m^{-3}. The average velocities of *P* and *S* waves for every sensor in the mine are estimated by the Institute of Mine Seismology (IMS) using calibration blasts. Previous studies (Hallo & Gallovič 2016; Pugh *et al.* 2016) show that mismodelling of the velocity structure may induce impact on the obtained focal mechanism solutions. In case of Kiruna mine, the preliminary results of the tomography suggest a low variability of rheological parameters in the foot wall and a main heterogeneity—the ore body. It appears that a homogeneous velocity model is a good first order approximation to the underground structure if both the seismic sources and the seismic sensors are both in the foot wall, which is the case for most of the seismic sources.

3.2 Moment tensor inversion method

When starting an MT inversion, we assume that the hypocentral location and the origin time are known. The duration of the rupture process is fixed to the length of four samples (0.02 s). This duration was obtained after testing a range of possible durations. A spatial filter is applied to select sensors only located in a desired range of epicentral distances (here 100–600 m). The inversion is performed at different steps, following Cesca *et al.* (2013).

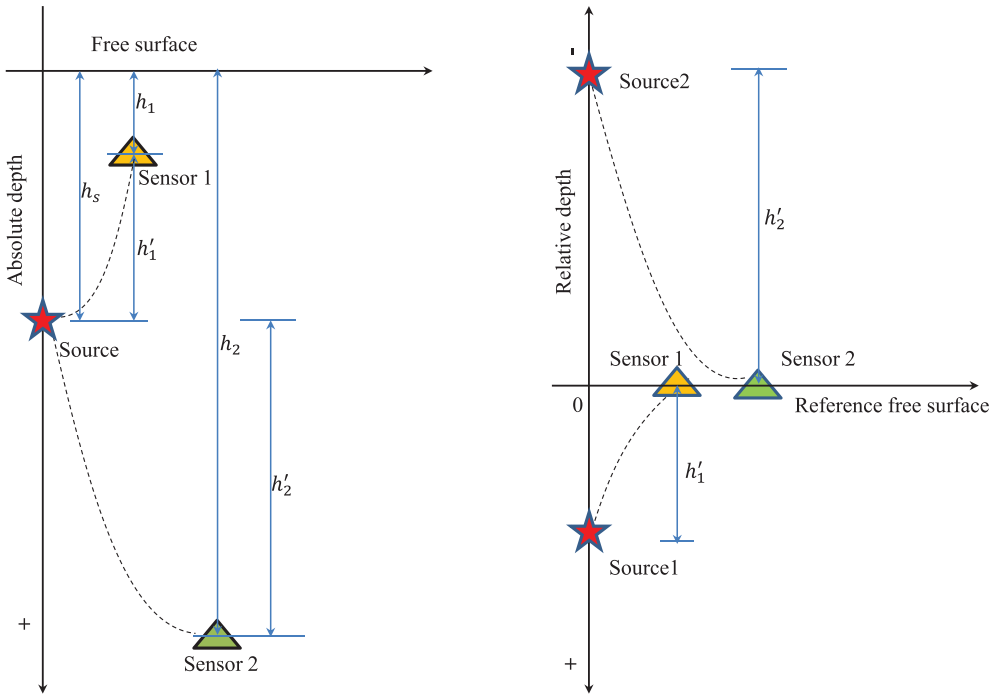

Figure 2. Schematic diagram showing the relative depth calculation for GFDB with sensors located at different depths. Left: in the real configuration, absolute depths of source and sensors are expressed with respect to the free surface. Right: in the implemented equivalent configuration, all sensors are located at a common 'reference free surface', and the source is located at relative depths h_i' with respect to each sensor i .

Table 1. Details of the configuration of the GFDB.

Sample rate (Hz)	Sensor depth (m)	Min source depth (m)	Max source depth (m)	Source depth delta (m)	Min distance (m)	Max distance (m)	Distance delta (m)
200	0	−300	500	10	10	5000	10

In the first step, the inversion relies on the fit of amplitude spectra. The advantage of working in the frequency domain lies in the higher stability and lower dependency on the alignment of the observed seismograms due to mismodelling of the geological structures and poorly known velocity model (Dahm & Krüger 1999; Cesca *et al.* 2006). A bandpass filter is applied to the data in order to keep the flat part of the *P*- and *S*-wave spectra. A taper is applied to obtain only the signal corresponding to the *P*- and *S*-wave part of the seismograms. The taper is chosen based on theoretical calculations of the seismogram length and theoretical first arrivals, knowing the source–receiver geometry and the chosen velocity model. Synthetic seismograms are calculated and their amplitude spectra are obtained. The point source parameters are retrieved using a non-linear inversion algorithm. The misfit (Cesca *et al.* 2006) between the synthetic and observed spectra for one component waveform is calculated using a L2 norm and normalized against the zero-trace.

The best DC solution and a number of strong non-DC solutions constitute the set of the starting source configurations for the FMT inversion. The FMT inversion is performed similarly to the pure DC inversion, by fitting the amplitude spectra. The first inversion step is successfully completed when both a DC model (parameterized by centroid location, centroid time, scalar moment, magnitude, strike, dip and rake) and the FMT model (centroid location and time, FMT configuration and decomposition) have been obtained. However, the amplitude spectra inversion cannot resolve the DC and FMT polarity.

In the second step, the polarity ambiguity is resolved by fitting the displacement traces in the time domain. The source location (centroid location) is also improved using the depth obtained in the first step. In this step, we use the same bandpass filter and taper that are applied in step 1. Synthetic waveforms are computed for the two possible polarities (both for the DC and FMT models) solutions. The synthetic and observed seismograms are cross correlated in order to align both time traces. The misfit in the time domain is computed again using the L2 norm. The comparison between the misfits of the two possible types of quadrants allows solving the MT polarity. The best centroid location is retrieved after a grid search with several perturbations of latitude, longitude and origin time. The polarity is similarly resolved for the best FMT solution; an FMT decomposition, through DC, CLVD and ISO components is then performed (Cesca *et al.* 2013).

4 PERFORMANCE TESTS WITH SYNTHETIC DATA

The inversion method and its implementation were tested on synthetic data to assess the MT resolution against several factors. In particular, the reliability of the method and inversion stability were tested: (1) for different azimuthal and 3-D network coverage, (2) to assess the effect of seismic noise contamination, (3) upon the assumption of inaccurate source parameters (epicentral location, depth and origin time) and (4) to find the minimum number of sensors that guarantee reliable results. These tests also helped to

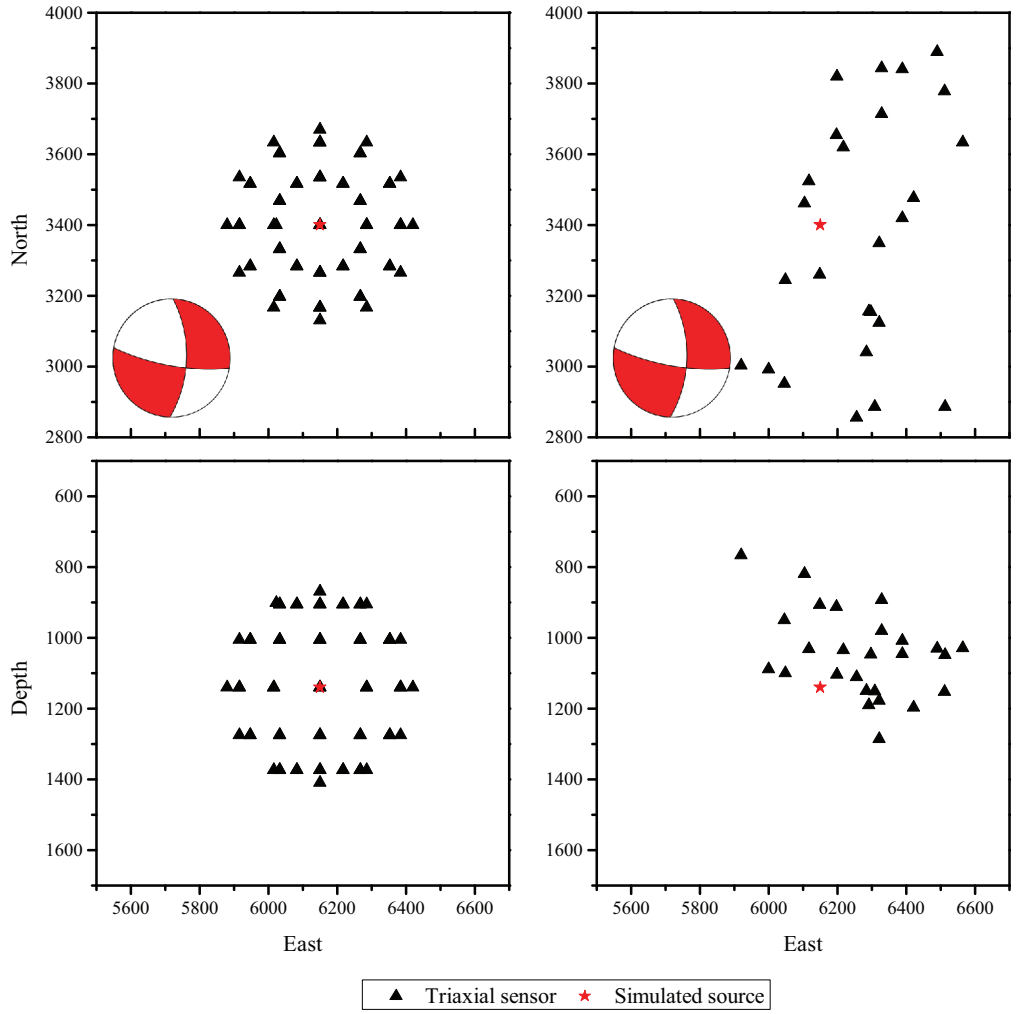

Figure 3. 2-D planar view of the source–sensor geometry used for synthetic data tests in map view (top) and east–west vertical section (bottom), for the imaginary spherical network (left) and the real network (right). The source locations are marked by red stars and sensors by black triangles. The beach-ball diagrams show the chosen source mechanism.

Table 2. Parameters of the simulated source (*X*, *Y* and *Z*—in mine coordinate system).

X	*Y*	*Z*	Strike	Dip	Rake	Moment magnitude
6150	3400	1140	100.0°	75.0°	−150.0°	−0.2

demonstrate the functionality and specific features of the inversion routine. Whereas quantitative results of these synthetic tests may not be extrapolated to other networks and seismicity cases, our procedure provides an example of good practice for the assessment of MT inversion stability in mining environments. In this case, the procedure is limited only to four factors listed above and does not include the uncertainties in the medium and the corresponding Green's function evaluation.

The synthetic performance tests were carried out for two different network configurations, with sensors located on an ideal spherical surface (spherical network) surrounding the hypocentre and with sensors located at real locations of the monitoring system at Kiruna mine (Fig. 3). A point source with a pure shear mechanism (DC), typical for the mine, is chosen to create synthetic waveforms (source parameters are listed in Table 2). The chosen source geometry corresponds to the inversion result of one of the historic events in block #33/34. A set of synthetic waveforms was created for both network configurations.

4.1 Inversion performance for synthetic data from spherical network

The adoption of a spherical network aims to assess and quantify the uncertainties and instabilities of the inversion procedure depending on the network coverage. The results also provide information about the minimum number of sensors that could be used to get reliable results.

For the spherical network the source is located at the centre of the sphere, which has a radius equal to 270 m. We used a total of 62 sensors located at regular angular distance (every 30°), thus providing a complete coverage of the focal sphere to avoid spurious influence of network asymmetries on the outcome of the inversion. The sensors were placed at seven different depths (from 270 m above

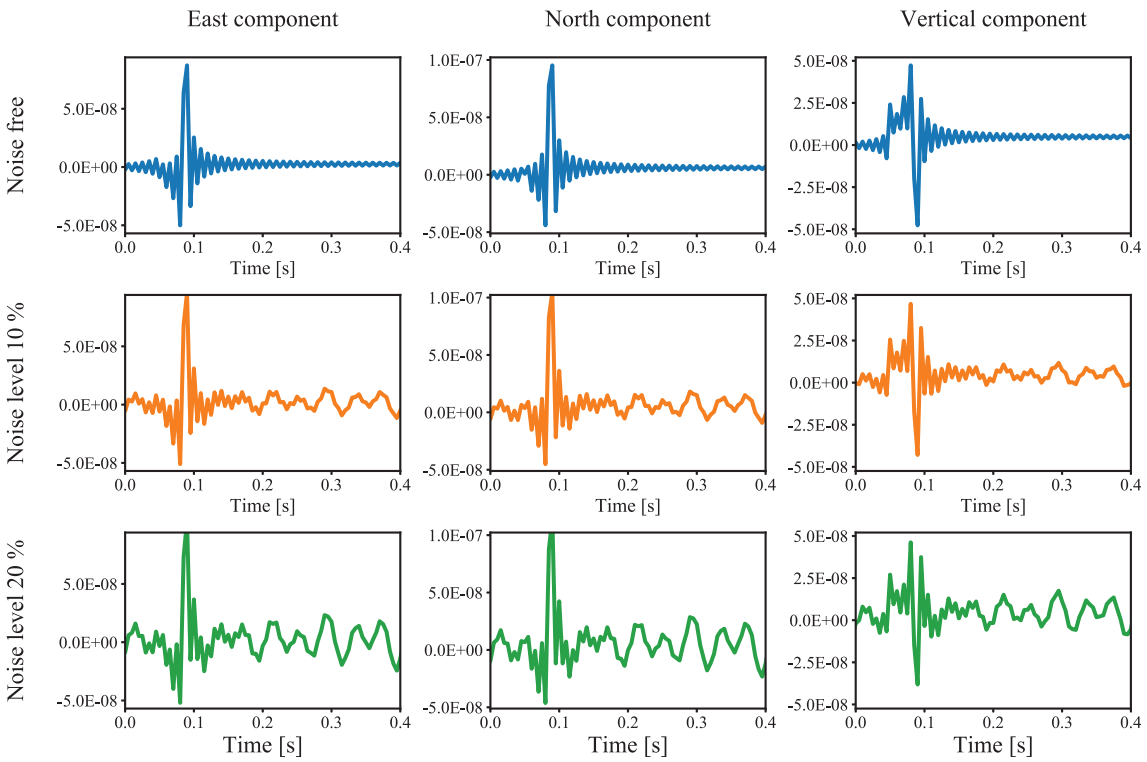

Figure 4. Example of synthetic waveforms for one sensor of the spherical network with different noise levels: noise-free data (top), noise level at 10 per cent (middle) and noise level at 20 per cent (bottom). The waveforms do not only show pulses for *P* and *S* waves, but also a ramp between *P* and *S*, which is a peculiar feature of near-field seismograms.

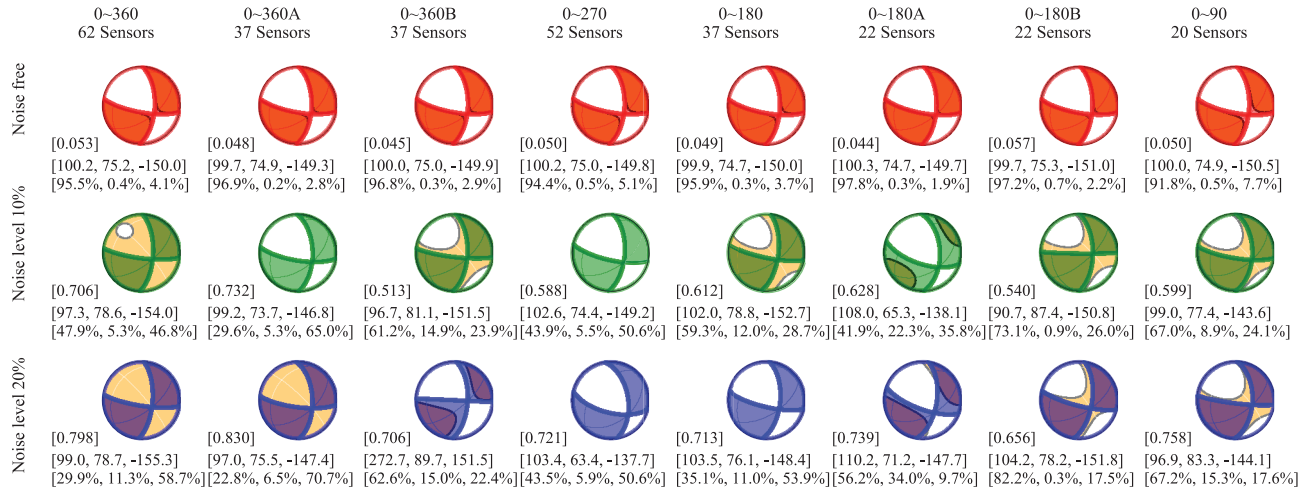

Figure 5. Inversion results with different azimuth and 3-D coverage of the sensors, as well as variable noise levels in the spherical network. The inversion result of the full moment tensor is plotted with beige colour filled in the compressional quadrants. The result of the pure DC is plotted with red line for noise free cases, green line for noise level 10 per cent cases and blue line for noise level 20 per cent cases. The azimuthal coverage and the corresponding number of sensors are shown at the top of the figure. The cases ending with 'A' and 'B' are for sensors only above the source and only below the source, respectively. The fault plane solutions (in format [strike, dip, rake]) and the decomposition of the full moment tensor (in format [DC, CLVD, ISO]) are listed below each beach-ball diagram.

the source to 270 m below it). The spherical network configuration is illustrated in Fig. 3. At the subsequent tests the spatial sensor coverage was progressively decreased, by reducing sensor number down to 52, 37, 36 and 20, and the azimuthal coverage to 0–270°, 0–180° and 0–90°. The inversion was also tested using sensors only above and only below the source.

After the 'noise-free' tests the synthetic waveforms were contaminated with additive real noise. First, the noise data were scaled relative to the maximum amplitude of each trace and then the magnified noisy data were added to the traces. We tested two different noise levels: 10 and 20 per cent (Fig. 4).

The inversion was carried out by fitting *P* and *S* waveforms, for a time window of 0.5 s, starting 0.2 s before the theoretical phase onset. The bandpass filter was set as 15–30 Hz. A taper was applied in the time domain, smoothing the time window on both sides. In this test, the source location, the source depth and the source origin

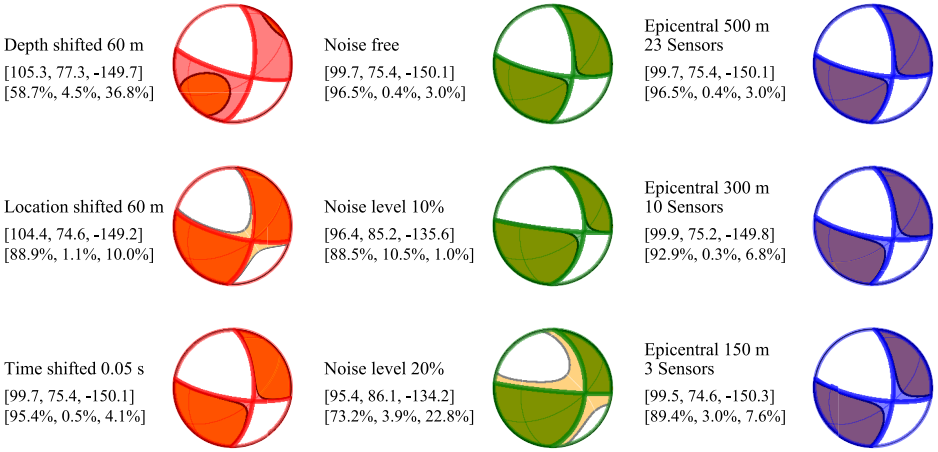

Figure 6. Inversion results assuming perturbed seismic hypocentre and origin time: left column, from top to bottom—depth, location and origin time perturbation, respectively; central column—for different noise conditions, from top to bottom with increasing the noise level; right column—for real network configurations, from top to bottom with reducing the maximal epicentral distance, the number of sensors and the azimuthal coverage. Full moment tensor inversion results are plotted with beige colour filled in the compressional quadrants, while the results for using a DC constrained are plotted with red lines (source parameter shift test), green lines (noise level test) and blue lines (epicentral distance test). The misfit, the fault plane solutions (in format [strike, dip, rake]) and the decomposition of the full moment tensor (in format [DC, CLVD, ISO]) are listed next to each beach-ball diagram.

Table 3. Source parameters of the eight selected events from mining block #33/34. The locations, corner frequencies, seismic moment and energy are routinely calculated by IMS.

No.	Data–time	Location/*X Y Z*	Corner frequency (Hz)	Seismic moment (N m)	Moment magnitude	Seismic energy (J)
1	2015.09.06–11:14:52.000	6444.8 3334.8 1133.6	71.7	2.32e + 09	0.20	2.91e + 03
2	2015.09.06–11:50:54.107	6397.9 3321.6 1103.8	110.0	7.57e + 08	0.12	1.07e + 03
3	2015.09.07–00:14:12.240	6349.4 3324.5 1070.9	68.6	1.73e + 09	0.12	2.42e + 03
4	2015.09.23–10:57:38.385	6402.6 3350.1 1151.8	38.7	3.11e + 10	0.96	1.49e + 05
5	2015.10.28–07:10:20.670	6350.8 3293.3 1087.5	82.9	1.80e + 09	0.13	2.63e + 03
6	2015.10.29–20:25:10.716	6408.9 3302.5 1097.2	75.7	3.98e + 08	−2.85	4.63e + 01
7	2015.10.30–06:12:36.144	6329.8 3273.0 1078.8	55.9	3.23e + 09	0.30	3.19e + 03
8	2016.01.22–17:12:15.050	6414.8 3359.4 1103.5	59.4	1.49e + 09	0.08	7.61e + 02

Table 4. Inversion results of the eight events using a bandpass of 15–30 Hz after noisy data were excluded. The results obtained from the DC component are presented for both possible nodal planes. The MT is decomposed into isotropic (ISO) and deviatoric components, and the latter one into double-couple (DC) and CLVD.

	Number of sensors		DC Plane 1			DC Plane 2			Decomposition of FMT (per cent)		
No.	All	Noisy data excluded	Strike	Dip	Rake	Strike	Dip	Rake	DC	CLVD	ISO
1	14	8	213.5	80.0	160.7	307.0	71.0	10.6	79.0	21.0	2.0
2	15	13	231.3	28.5	−15.2	334.8	82.8	−117.7	45.0	55.0	56.0
3	15	13	296.9	82.1	113.1	44.9	24.3	19.6	80.0	20.0	73.0
4	13	11	35.9	68.9	160.2	133.3	71.5	22.3	61.0	39.0	33.0
5	15	14	35.2	70.5	160.4	132.0	71.6	20.6	83.0	17.0	32.0
6	14	5	345.8	60.9	−131.7	227.2	49.3	−39.9	57.0	43.0	41.0
7	14	11	268.0	14.6	19.7	158.9	85.1	103.8	51.0	49.0	25.0
8	10	6	132.6	36.8	−102.5	328.0	54.2	−80.8	62.0	38.0	14.0

time were fixed to their correct values. The three tests (without and with noise at level 10 and 20 per cent) were performed with the same input parameters and inversion configurations. The results are shown in Fig. 5

Results show that the pure DC and FMT solutions can be correctly retrieved for the noise-free data, even with the poorest spatial coverage (azimuthal coverage 0∼90°). Using noise contaminated data (Fig. 5, centre and bottom rows), the pure DC inversion results remain very stable with small misfit, and the number of sensors, azimuthal coverage and 3-D geometry combined with an increasing noise level have little influence on the pure DC resolution. However, the FMT inversion results are more sensitive to the seismic noise and spatial coverage, which results in spurious non-DC term contamination of the resolved FMT.

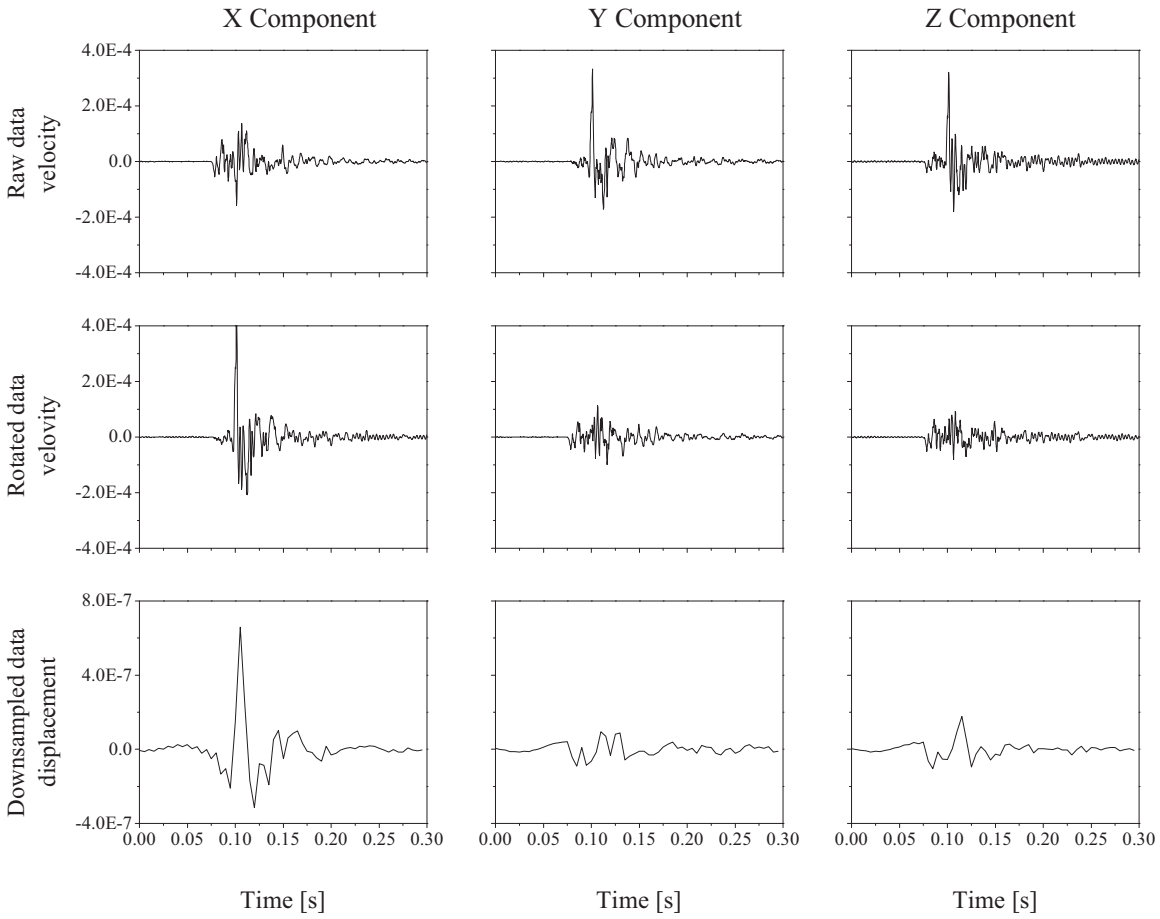

Figure 7. Example of waveforms recorded by sensor #0253 (distance 233 m) for event 2015.09.06–11:14:52 (#1 in Table 3). Top: raw velocity data with sampling rate 6000 Hz. Centre: rotated velocity data with sampling rate 6000 Hz. Bottom: final displacement data with sampling rate 200 Hz.

4.2 Inversion performance with synthetic data for Kiruna mine seismic system configuration

The Kiruna mine seismic network follows the mining operations and the sensors are installed around the ore body (Fig. 1). In this way, the 3-D coverage is very limited in a direction perpendicular to the ore body. The test with the real network was carried out to test the performance of the method with the geometrical limitations of the real network configuration at Kiruna mine. In these tests, the independent effects of the referenced input source parameters, noise levels and the epicentral distance will be considered.

First, the dependence of the inversion results upon the accuracy of the adopted hypocentre location/origin time is tested with noise-free data, considering sensors only with hypocentral distances up to 500 m (23 sensors). Then three scenarios were considered: we separately assumed a source depth shift of 60 m (considering a depth of 1200 m instead of the correct value of 1140 m), a lateral source location shift of 64 m (correct values 6150 m and 3400 m in X and Y coordinates but using 6192 m and 3443 m, respectively) and a source origin time shift of 0.05 s (assuming a 0.05 s delay with respect to the true origin time).

The dependence on noise conditions was then tested assuming the correct hypocentre location/origin time for the following three scenarios: noise-free data, 10 and 20 per cent noise level. Again, we used data from 23 sensors with maximum hypocentral distance of 500 m.

At last, the hypocentral distance requirement was tested with the chosen source model (Table 2) and with noise-free data. This test consisted of three scenarios: maximum distance of 500 m (23 sensors), 300 m (10 sensors usable) and 150 m (only three sensors).

Every inversion in this section was carried out using the same inversion setup described in Section 4.1, in terms of tapering, frequency range and inversion procedure. The inversion results of the synthetic data are shown in Fig. 6. Results show that the DC source parameters were correctly retrieved in all tests with noise-free data, even with only three observations or for spatial and temporal shifts of the seismic source. The strike of the nodal plane is rotated only by 5° in the case of the depth shift, 4° in the case of the location shift and no rotation was observed in the case of a time shift. Only the depth shift had an essential effect on the retrieved FMT, with a large ISO component (36 per cent) appearing as an artefact.

The DC source parameters appear very sensitive to noise levels. A noise level of 10 or 20 per cent is sufficient to rotate the nodal plane more than 12°. The noise affects also the other components of the FMT, resulting in 21 per cent ISO and up to 23 per cent CLVD components.

In case of noise-free data, a decrease of the number of sensors and a poorer azimuthal coverage have a negligible effect on the resolved fault plane solution. Small ISO component appears as an artefact with decreasing the number of sensors, reaching 10 per cent when only three sensors were used.

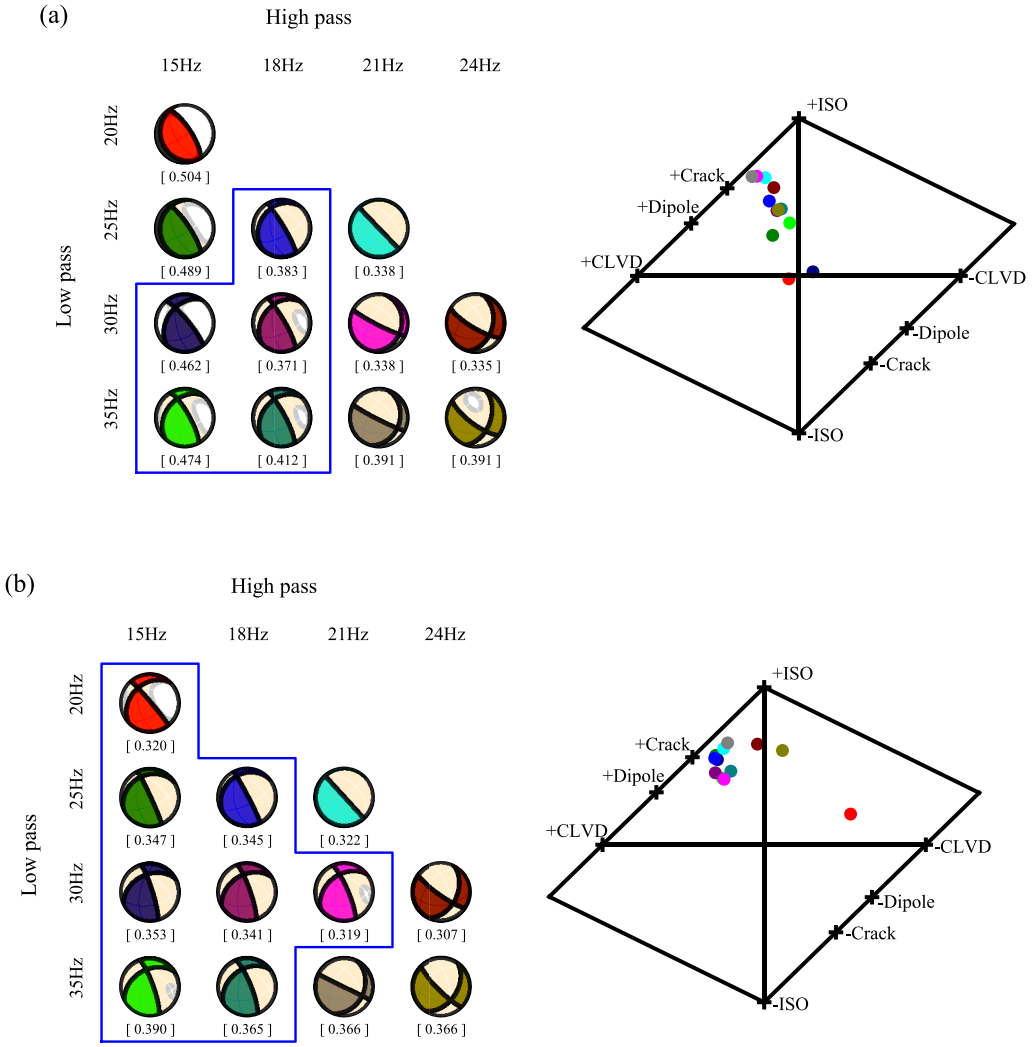

Figure 8. Moment tensor inversion results for the event 2015.09.06–11:50:54 (#2 in Table 3) obtained for different bandpass filter ranges: (a) MT result with all recorded data and (b) MT results without noisy data. The beach balls with the DC component (thick lines) and the FMT (thin lines, circle inside some of the coloured area) are shown on the left. The Hudson source type diagrams of the FMT are shown on the right. The results presented with same colour correspond to the same bandpass range. The misfit values of the solutions are shown below each beach ball. Solutions of similar type are encircled by a blue line.

In conclusion, the results from this test show that the FMT inversion result appear mostly sensitive to the source depth and the noise level. In these cases, the DC source parameters are affected by rotation of the nodal planes up to 12° and significant spurious non-DC (mostly ISO) components appearing.

5 APPLICATION—REAL DATA INVERSION

5.1 Mining activity and seismic data

MT inversion was carried out also for real seismic events, recorded in Kiruna mine. Eight events with moment magnitude ranging from 0.0 to 1.0 were selected for this test. The events, listed in Table 3, are located in the mining block #33/34. The waveform data are obtained from the mining microseismic monitoring system described in Section 2. We considered only data from triaxial geophones.

The original velocity data are recorded with a 6000 Hz sampling. The data pre-processing consisted of four main steps. First, the waveform data were converted from ASCII to miniSEED format. Second, a removal of the mean and trend was performed. Third, the traces were rotated to the north–south, east–west and vertical reference system. For this aim, the orientation of the triaxial sensors calculated by IMS from calibration blasts was used. Finally, the instrument response was corrected, the data were integrated to displacement and downsampled to 200 Hz. An example of the recorded waveforms before and after pre-processing is shown in Fig. 7.

5.2 Testing the moment tensor inversion with selected real data

MT inversion requires fitting spectra and waveforms within the frequency band of the flat low-frequency asymptote of the event spectra (below the corner frequency) and within it in the range where the signal-to-noise ratio is the largest. Furthermore, we need to use frequencies as low as possible, as they are less affected by unknown structural heterogeneities. The events selected for this study have different magnitudes and their corner frequencies vary from ∼40 to

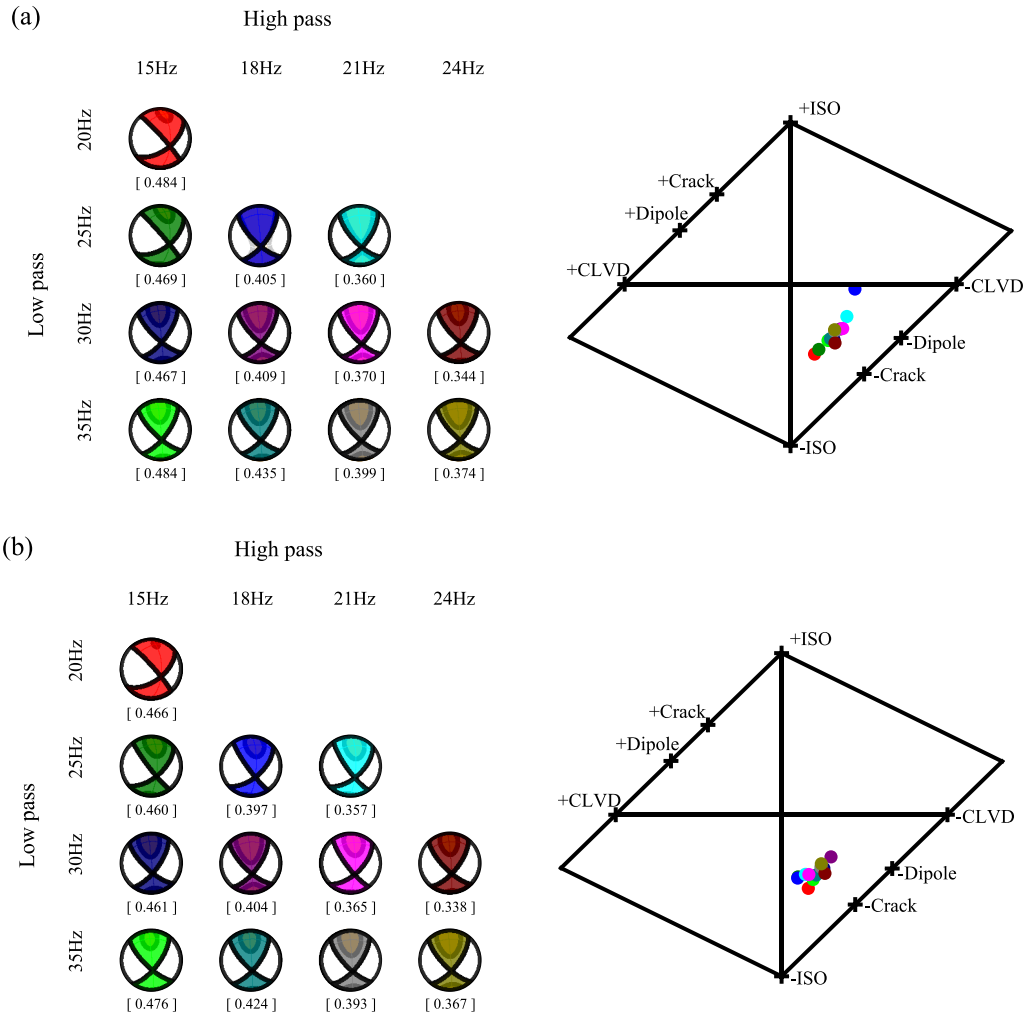

Figure 9. Moment tensor inversion results for the event 2015.09.23–10:57:38 (#4 in Table 3) obtained for different bandpass filter ranges: (a) MT results with all recorded data; (b) MT results without noisy data. The beach balls with the DC component (thick lines) and the FMT (thin lines, circle inside some of the coloured area) are shown on the left. The Hudson source type diagrams of the FMT are shown on the right. The results presented with same colour correspond to the same bandpass range. The misfit values of the solutions are shown below each beach ball.

∼110 Hz (see Table 3). We thus tested different bandpass ranges in different cases.

The bandpass ranges were constrained between the highest natural frequency of the sensors (14 Hz, Section 2) and the lowest corner frequency of the studied real events (38.7 Hz, Table 3). The MT inversion was repeated for several different frequency ranges, for a combination of minimum frequency ranging from 15 to 24 Hz and maximum frequency from 20 to 35 Hz.

Same as for the synthetic tests, we fit a window of 0.5 s for the real data, starting 0.2 s before the first *P* arrivals, tapered at both sides. The source location, depth and origin time were set according to Table 3. They were calculated by IMS. The inversion process is analogous to the one described for synthetic data (see Section 4).

Two cases of the MT inversion were considered for every event: (1) using all available waveform data up to hypocentral distance 600 m and (2) excluding waveforms with noise levels larger than 20 per cent; the noise level is estimated by comparing the root mean square of the noise window (0.5 s before *P* arrival) and the signal window (0.5 s after *P* arrival, which for our data includes *P* and *S* waves). The stability of the pure DC solution and the type of the FMT obtained for different bandpass filters were compared for all these cases.

Fig. 8 shows the results for the event 2015.09.06–11:50:54 (#2 in Tables 3 and 4, M_W 0.1, f_c 110 Hz). For this event, in case of inversion with all data (including 15 sensors with low noise level and two sensors with noisy data) a comparatively stable DC solution and FMT are observed for a variety of bandpass filters (shown in Fig. 8a, left). The cases with narrower bandpass filters (end cases with ranges 15–20, 21–25, 24–30, 21–35 and 24–35 Hz) make exception (visible on the Hudson diagram as points outside of the cluster of most solutions). The mechanism type for most of the cases is oblique-normal while for the end cases varies between oblique-reverse and pure dip-slip. The estimated moment magnitude ranges from 0.09 to 0.12, with lower magnitudes estimated when fitting lower frequencies. Our results suggest that FMT instabilities affect more the ISO than the CLVD component (Fig. 8a, right). This result differs from previous studies (e.g. Horálek & Šílený 2013; Stierle *et al.* 2014), which reported larger uncertainties for the CLVD component.

Removing the noisy traces (only two sensors) showed more stable results for the FMT (Fig. 8b, left) although the solutions for

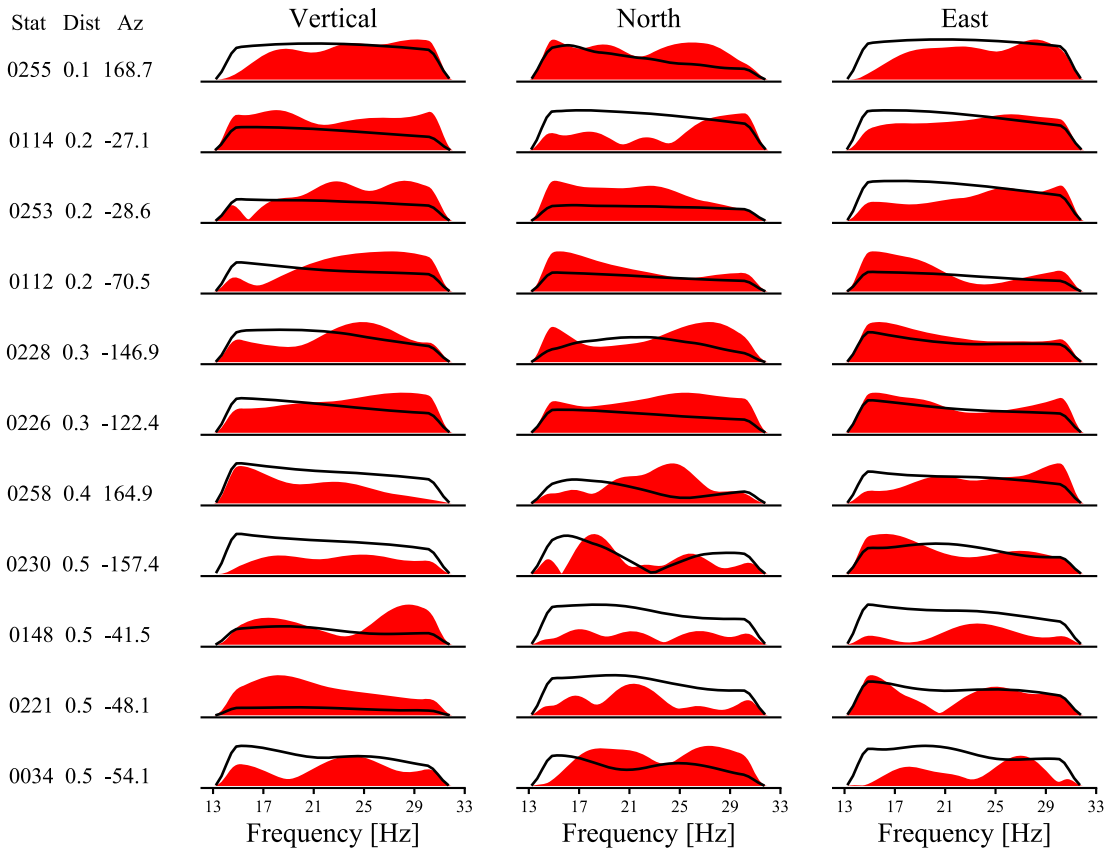

Figure 10. Fit of amplitude spectra with bandpass 15–30 Hz of event 2015.09.23–10:57:38 (#4 in Table 3). Observed amplitude spectra (red areas) are compared to synthetic ones (black lines) for the 11 sensors. The sensor name, epicentral distance (m) and azimuth are shown on the left side.

most of the narrower bandpass filter cases were also different. The resolution of focal mechanism (DC) changed in a similar way as for the previous case when noisy data were considered. Consistent full MT solutions were obtained for most of the bandpass filters, where different solutions form a tight cluster on the Hudson diagram (Fig. 8b, right). The exceptions are, again, only the cases with narrow-bandpass filters.

The analysis of these results shows that the adoption of narrow bandpass filters, at the edges of the initially chosen frequency band for testing (15–35 Hz), leads to unstable DC results and large spurious ISO components. On the contrary, it seems that bandpass filters 15–25 or 15–30 Hz give more stable results and could be used for routine determination of the FMT.

Fig. 9 shows the inversion results for the event 2015.09.23–10:57:38 (#4 in Table 3, M_W 0.96, f_c 39 Hz). This is the event with the highest moment magnitude and the lowest corner frequency (Table 3). For this event we used data from 13 sensors, two of them had traces with high noise. For this event, the pure DC solutions showed a stable oblique-reverse mechanism (Fig. 9a, left). Removing the noisy data had a marginal effect on the results for all bandpass filters (Fig. 9b, left). The notable improvement is in the FMT decomposition (Fig. 9b, right). The solutions for all bandpasses form a nice tight cluster on the Hudson diagram, compared to the solutions with the noisy data included (Fig. 9a, right). The fit of amplitude spectra and displacement traces in pure DC inversion with bandpass 15–30 Hz (poor data excluded) for this event are shown in Figs10 and 11, respectively.

In conclusion for this case, it was found that the bandpass filter had a negligible influence on the DC and FMT inversion result, but removing the noisy data improved the consistence of the MT solutions for all bandpass cases.

5.3 Moment tensor results with real data and discussion

As a result from the analysis for all cases in Table 3, we found that for a routine inversion of the FMT, a bandpass of 15–30 Hz could be used to obtain reliable results for events of all magnitudes. The results in this frequency band for all events, after excluding the noisy data, are shown on Fig. 12 and listed in Table 4.

If we consider only the DC component of the FMT, three of the events are of predominantly normal type, two of them of predominantly reverse type and the rest—with predominant strike-slip component. The strike of the nodal planes varies but there are two distinctive orientations around 30°–50° and 310°–340° (most of the orientations; Fig. 13a). The dip of the planes also varies but the majority is within 60°–90° (Fig. 13b). The mechanism of the FMT also varies (Fig. 14). Some of the events correspond to opening cracks and some to closing cracks (Fig. 14). The orientation of the ore body is roughly N–S, dipping east ∼60°. The orientations of the nodal planes are not exactly N–S but many of them are around it, varying from NNW to NNE with a dip along the ore body or in the opposite direction.

It should be noted that the solutions for the DC component obtained from the FMT inversion in some cases are different from the solutions assuming pure DC (events #2, #3 and #5; Fig. 12). There are some variations in the strike and dip orientation for the other cases but the type of the mechanism remains the same. One possible reason for the large discrepancies between two types of solutions

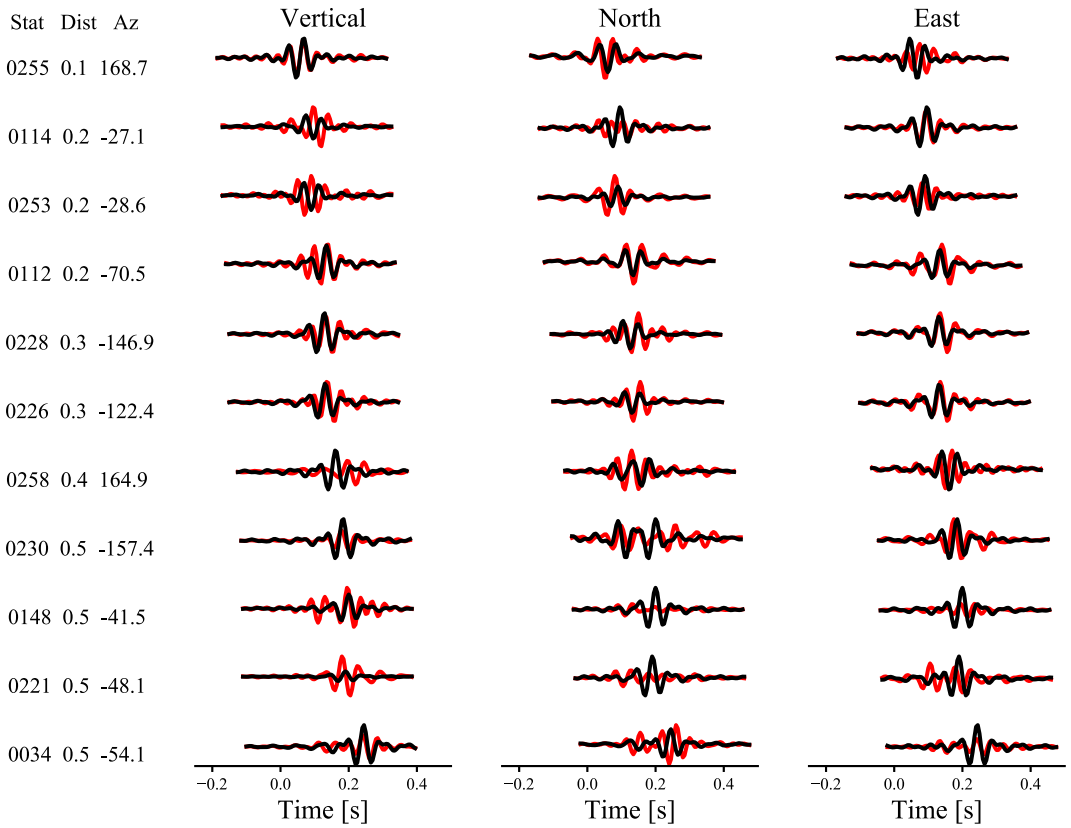

Figure 11. Fit of observed (red) and synthetic (black) seismograms with bandpass 15–30 Hz of event 2015.09.23–10:57:38 (#4 in Table 3) for the 11 sensors. The sensor name, epicentral distance (m) and azimuth are shown on the left side.

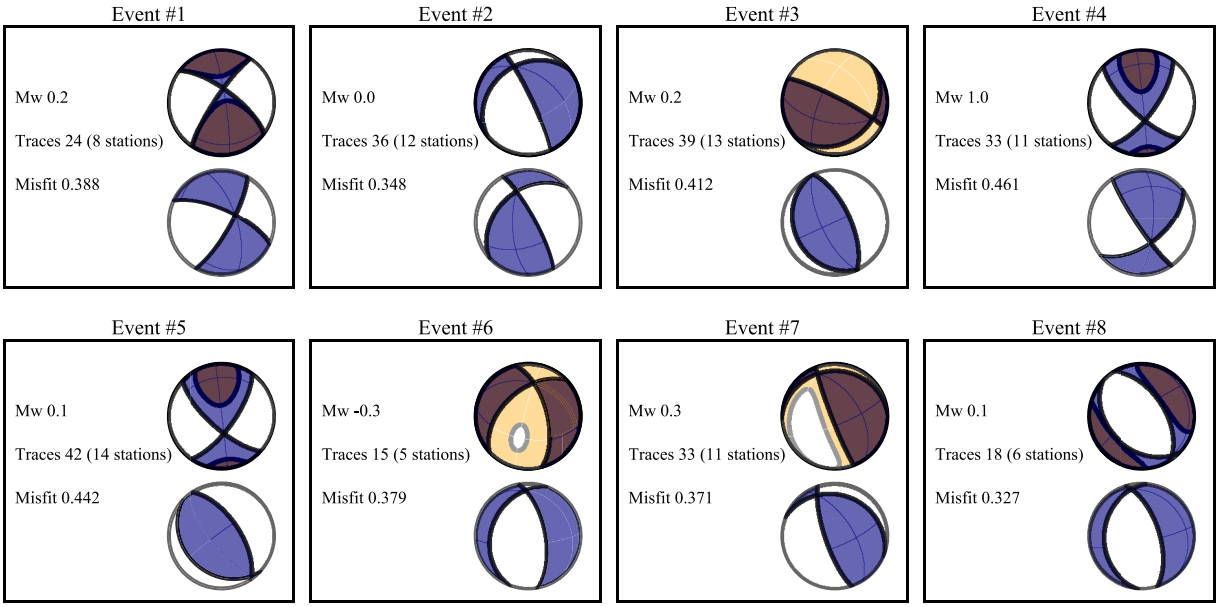

Figure 12. Moment tensor inversion results for the events listed in Table 3 with bandpass 15–30 Hz. The information for the bandpass filter, the number of traces, the calculated moment magnitude and the misfit value are displayed at the left side of each subfigure. The upper beach ball shows the FMT (in light beige colour) with the DC solution decomposed from the FMT. The lower beach ball shows the solution from pure DC inversion.

would be a large non-DC component (Guilhem *et al.* 2014). Indeed, for events #2 and #3 the ISO components are the largest ones, 56 and 73 per cent, respectively (Table 4). The CLVD component is also large for event #2 (55 per cent of the deviatoric component). For event #5 the ISO component was found to be 32 per cent, also one of the larger ones. This shows that if a large non-DC component is expected, direct inversion using pure DC could give false results and should be used with caution.

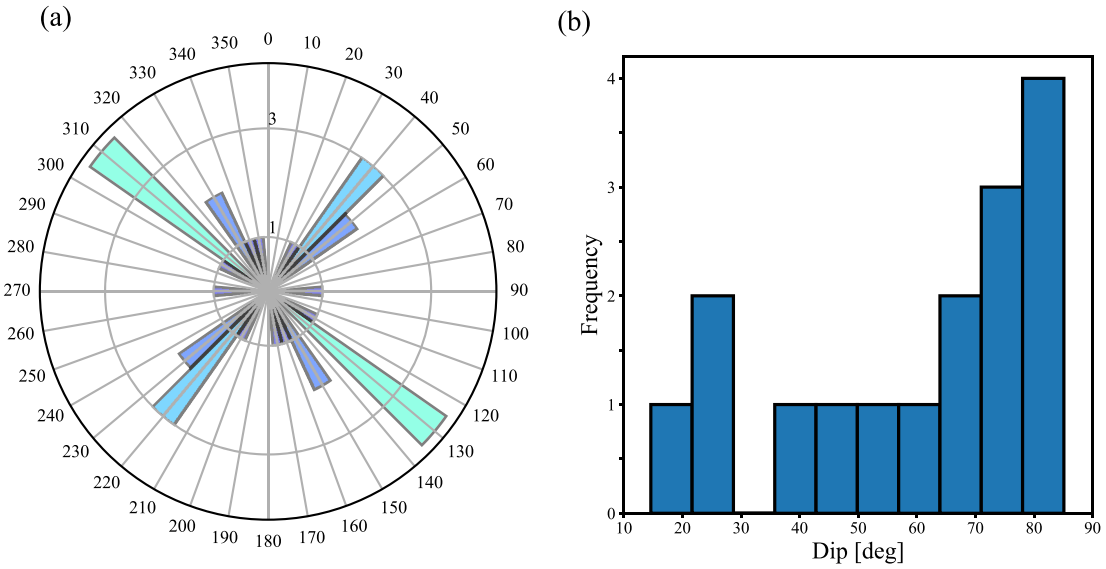

Figure 13. (a) Rose diagram of the nodal plane strikes obtained for the DC component of the FMT for the eight real events (Table 3) and (b) histogram with the dip for the same planes

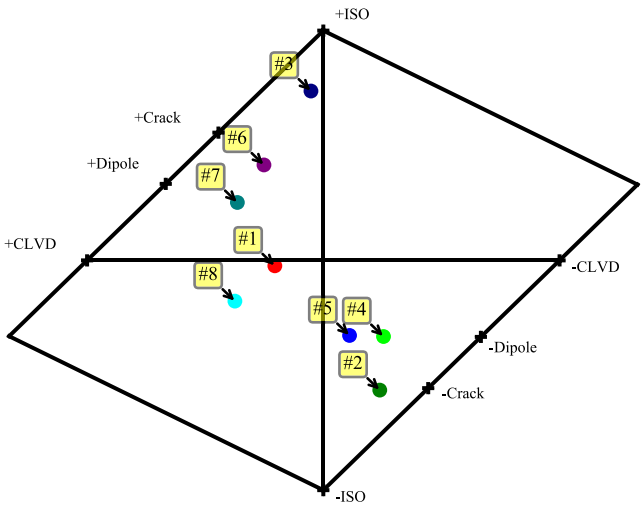

Figure 14. Hudson source-type diagram for all eight real events (Table 3)

Besides the MT, we also tested the performance of the routine for the scalar moment and moment magnitude. The moment magnitudes calculated by our MT inversion tools and by IMS based on spectral analysis are compared in Fig. 15, showing a good agreement.

6 CONCLUSION

In this work, we adapted and tested waveform inversion method on high frequency data recorded by a dense underground seismic system in one of the largest mines in the world (Kiruna mine, Sweden). First, we constructed a GFDB using a homogeneous velocity model, assuming 3-D distribution of potential sources and receivers. A set of MT inversions using synthetic data were carried out to test the effects of different factors on MT inversion stability and source parameters accuracy, including the network spatial coverage, the number of sensors and the signal-to-noise ratio. The influence of the accuracy of the input source parameters on the inversion results was also tested.

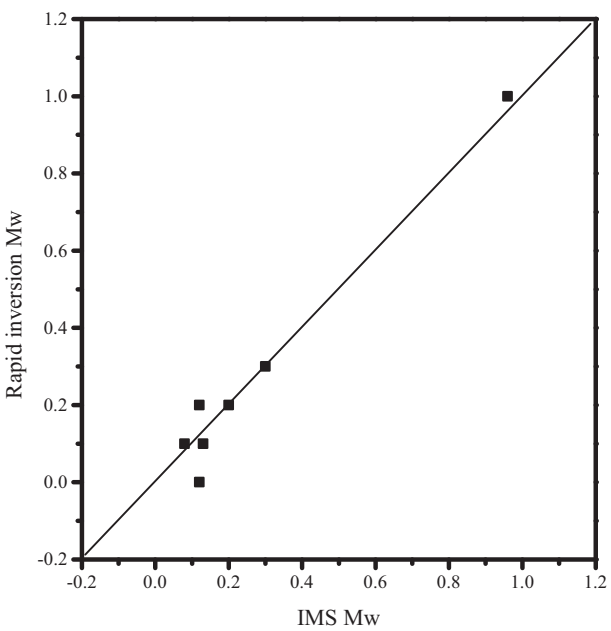

Figure 15. Comparison of moment magnitude M_W estimates by IMS and Kiwi tools.

Tests with synthetic data were carried out for two different seismic network configurations, with sensors located on a spherical surface (spherical network) surrounding the hypocentre and with sensors located at real locations of the monitoring system at Kiruna mine. A point source with a pure shear mechanism (DC) was used to create synthetic waveforms, corresponding to a real historic event. It was found that the fault plane solutions can be retrieved correctly when noise-free data were used, even with the poorest spatial coverage. The major artefact found in these cases of noisy data were large ISO component and some CLVD component.

The MT inversion methodology was applied on data from eight events chosen from mining bersion in some cases are different from the solutionlock #33/34 at Kiruna mine (moment magnitude range 0.1–1). Source parameters including scalar moment, magnitude,

DC, CLVD and ISO contributions as well as the strike, dip and rake configurations of the DC term were obtained. It was found that the noise level had a significant influence on the MT reliability for some cases, especially for narrow bandpass filtered data. A bandpass filter 15–30 Hz was found to give reliable solutions for studied events and is recommended to be used for routine work. The orientation of the ore body is roughly N–S, dipping east ∼60°. The orientations of the nodal planes in most cases vary from NNW to NNE with a dip along the ore body or in the opposite direction.

ACKNOWLEDGEMENTS

We wish to thank Thomas Wettainen from LKAB for his detailed and constructive comments. Funding for this study was provided by the Hjalmar Lundbohm Research Centre (HLRC) and LKAB (Sweden), as well as Centre of Advanced Mining and Metallurgy (CAMM).

REFERENCE

Aid, K. & Richards, P.G., 1980. *Quantitative Seismology: Theory and Methods,* W. H. Freeman and Co.

Cesca, S., Battaglia, J., Dahm, T., Tessmer, E., Heimann, S. & Okubo, P., 2008. Effects of topography and crustal heterogeneities on the source estimation of LP event at Kilauea volcano, *Geophys. J. Int.,* **172**(3), 1219–1236.

Cesca, S., Buforn, E. & Dahm, T., 2006. Amplitude spectra moment tensor inversion of shallow earthquakes in Spain, *Geophys. J. Int.,* **166**(2), 839–854.

Cesca, S., Heimann, S., Stammler, K. & Dahm, T., 2010. Automated procedure for point and kinematic source inversion at regional distances, *J. geophys. Res.,* **115**(B6), doi:10.1029/2009JB006450.

Cesca, S., Rohr, A. & Dahm, T., 2013. Discrimination of induced seismicity by full moment tensor inversion and decomposition, *J. Seismol*., **17**(1), 147–163.

Dahm, T. & Krüger, F., 1999. Higher-degree moment tensor inversion using far-field broad-band recordings: theory and evaluation of the method with application to the 1994 Bolivia deep earthquake, *Geophys. J. Int.,* **137**(1), 35–50.

Dineva, S. & Boskovic, M., 2017. Evolution of seismicity at Kiruna Mine, in *8th Int. Conf. on Deep and High Stress Mining, Perth, 28–30 March 2017,* pp. 125–140, ed. Wesseloo, J., Australian Centre for Geomechanics.

Domingues, A., Custodio, S. & Cesca, S., 2013. Waveform inversion of small-to-moderate earthquakes located offshore southwest Iberia, *Geophys. J. Int.,* **192**(1), 248–259.

Dufumier, H. & Rivera, L., 1997. On the resolution of the isotropic component in moment tensor inversion, *Geophys. J. Int.,* **131**(3), 595–606.

Guilhem, A., Hutchings, L., Dreger, D.S. & Johnson, L.R., 2014. Moment tensor inversions of M∼ 3 earthquakes in the Geysers geothermal fields, California, *J. geophys. Res.,* **119**(3), 2121–2137.

Hallo, M. & Gallovič, F., 2016. Fast and cheap approximation of Green function uncertainty for waveform-based earthquake source inversions. *Geophys. J. Int.,* **207**(2), 1012–1029.

Harris, P.C. & Wesseloo, J., 2015. *mXrap software*, version 5, Australian Centre for Geomechanics, The University of Western Australia, Perth, Western Australia, http//:www.mXrap.com.

Horálek, J. & Šílený, J., 2013. Source mechanisms of the 2000 earthquake swarm in the West Bohemia/Vogtland region (Central Europe), *Geophys. J. Int.,* **194**(2), 979–999.

Jechumtálová, Z. & Šílený, J., 2005. Amplitude ratios for complete moment tensor retrieval, *Geophys. Res. Lett.,* **32**(22), doi:10.1029/2005GL023967.

Jost, M.U. & Herrmann, R.B., 1989. A student's guide to and review of moment tensors, *Seismol. Res. Lett.,* **60**(2), 37–57.

Julian, B.R., Miller, A.D. & Foulger, G.R., 1998. Non-double-couple earthquakes 1. Theory, *Rev. Geophys.,* **36**(4), 525–549.

Knopoff, L. & Randall, M.J., 1970. The compensated linear-vector dipole: a possible mechanism for deep earthquakes, *J. geophys. Res.,* **75**(26), 4957–4963.

Li, J., Zhang, H., Sadi Kuleli, H. & Nafi Toksoz, M., 2011. Focal mechanism determination using high-frequency waveform matching and its application to small magnitude induced earthquakes, *Geophys. J. Int.,* **184**(3), 1261–1274.

Nakamura, M., 2002. Determination of focal mechanism solution using initial motion polarity of *P* and *S* waves, *Phys. Earth planet. Inter.,* **130**(1-2), 17–29.

Pugh, D.J., White, R.S. & Christie, P.A.F., 2016. A Bayesian method for microseismic source inversion, *Geophys. J. Int.,* **206**(2), 1009–1038.

Sen, A.T., Cesca, S., Bischoff, M., Meier, T. & Dahm, T., 2013. Automated full moment tensor inversion of coal mining-induced seismicity, *Geophys. J. Int.,* **195**(2), 1267–1281.

Song, F. & Toksöz, M.N., 2011. Full-waveform based complete moment tensor inversion and source parameter estimation from downhole microseismic data for hydrofracture monitoring, *Geophysics,* **76**(6), WC103–WC116.

Stierle, E., Vavryčuk, V., Šílený, J. & Bohnhoff, M., 2014. Resolution of non-double-couple components in the seismic moment tensor using regional networks—I: a synthetic case study, *Geophys. J. Int.,* **196**(3), 1869–1877.

Vavryčuk, V., 2001. Inversion for parameters of tensile earthquakes, *J. geophys. Res.,* **106**(B8), 16 339–16 355.

Vavryčuk, V., 2015. Moment tensor decompositions revisited, *J. Seismol*., **19**(1), 231–252.

Vavryčuk, V. & Kühn, D., 2012. Moment tensor inversion of waveforms: a two-step time-frequency approach, *Geophys. J. Int.,* **190**(3), 1761–1776.